Stabilizing the Structure of LiCoPO4 Nanocrystals via Addition of Fe3+: Formation of Fe3+ Surface Layer, Creation of Diffusion-Enhancing Vacancies, and Enabling High-Voltage Battery Operation

Naohisa Okita, Kazuaki Kisu, Etsuro Iwama, Yuki Sakai, Yiyo Lim, Yusuke Takami, Moulay Tahar Sougrati, Thierry Brousse, Patrick Rozier, Patrice Simon, et al.

Stabilizing the Structure of $LiCoPO_4$ Nanocrystals via Addition of Fe^{3+}: Formation of Fe^{3+} Surface Layer, Creation of Diffusion-Enhancing Vacancies, and Enabling High-Voltage Battery Operation

Naohisa Okita,[†] Kazuaki Kisu,[†,‡] Etsuro Iwama,[*,†,‡] Yuki Sakai,[†] Yiyo Lim,[†] Yusuke Takami,[†] Moulay Tahar Sougrati,[∥,⊥] Thierry Brousse,[‡,∥,#] Patrick Rozier,[‡,∥,¶] Patrice Simon,[‡,∥,¶] Wako Naoi,[◆] and Katsuhiko Naoi[*,†,‡,§]

[†]Department of Applied Chemistry, [‡]Global Innovation Research Organization, and [§]Advanced Capacitor Research Center, Tokyo University of Agriculture and Technology, 2-24-16 Naka-cho, Koganei, Tokyo 184-8588, Japan

[∥]Réseau sur le Stockage Electrochimique de l'Energie, RS2E FR CNRS 3459, 80039 Amiens, France

[⊥]Institute Charles Gerhardt Montpellier (ICGM), UMR 5253, Université de Montpellier, CNRS, 34059 CEDEX 5 Montpellier, France

[#]Institut des Matériaux Jean Rouxel (IMN), UMR 6502, Université de Nantes, CNRS, rue Christian Pauc, BP50609, 44306 CEDEX 3 Nantes, France

[¶]CIRIMAT, Université de Toulouse, CNRS, INPT, UPS, 118 route de Narbonne 31062 CEDEX 9 Toulouse, France

[◆]Division of Art and Innovative Technologies, K & W Inc., 1-3-16-901 Higashi, Kunitachi, Tokyo 186-0002, Japan

Supporting Information

ABSTRACT: Factors affecting the cyclability of the Fe-substituted $LiCoPO_4$ ($LiCo_{0.8}Fe_{0.2}PO_4$, LCFP) material were elucidated, including both the structural and electrode/electrolyte stability. Electrochemical characterization of the synthesized LCFP nanoparticles lends clear evidence for improved electrochemical stability of LCP, as well as enhanced rate capability, with Fe^{3+} substitution. Surface analysis using X-ray photoelectron spectroscopy (XPS) and electron energy loss spectroscopy (EELS) suggest that Fe enrichment on the surface of LCFP occurs through the oxidation of Fe^{2+} into Fe^{3+} in the synthesis process. The Fe^{3+}-rich phase on the LCP surface enhances the stability of the delithiated phase, preventing oxidative reactions with electrolytes during high-voltage operation. This surface protection persists as long as the electrochemical reduction of Fe^{3+} is avoided by ensuring that the full range of operating voltages lie above the Fe^{3+}/Fe^{2+} redox potential. Our findings may offer new approaches to stabilize the structure of LCP and other high-voltage positive electrodes for use in 5 V-class Li-ion batteries.

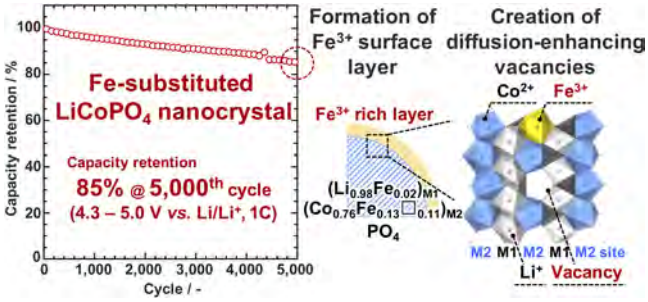

INTRODUCTION

Growing global demands for electric and hybrid electric vehicles necessitate the development of 5 V-class lithium ion batteries (LIBs) in view of their potential for higher specific energy and voltage compared with the 4 V-class LIBs. From this perspective, $LiCoPO_4$ (LCP) is an interesting material that offers advantages complementary to those of conventional cathode materials such as $LiCoO_2$ and $LiFePO_4$(LFP): high reaction potential of 4.8 V vs. Li/Li^+, theoretical capacity of 167 mAh g^{-1}, and thermal stability thanks to the P−O covalent bonding.[1−3] Although the low electron conductivity (<10^{-9} S cm^{-1})[4] and Li^+ diffusivity (<10^{-13} cm^2 s^{-1})[5] of LCP were initially thought to be problematic, it has since become clear that these difficulties can be remedied by controlling particle size/morphology,[6] doping metal ions,[7,8] carbon coating,[9] and/or synthesizing composites with conductive nanocarbons.[4,10] A more serious obstruction to practical utilization of LCP—and the primary focus of this study—is its poor cyclability: LIBs with LCP cathodes exhibit a dramatic decrease in capacity within just a few 10s of cycles. Mechanisms proposed to explain the plummeting capacity include instability of the ethylene carbonate (EC)-based electrolyte,[11] cleavage of P−O bonds by nucleophilic attack of F^- in $LiPF_6$-containing electrolytes,[12] and instability of the delithiated phase (Li_xCoPO_4, $x \ll 1$).[13,14] Formation of a protective surface film on LCP using alternatives to EC-based solvents, such as fluorinated ethylene carbonate[11] and other electrolyte additives,[15] has succeeded in prolonging useful life to 100 cycles. Allen et al. recently showed that Fe substitution into LCP in combination with a phosphite electrolyte additive

DOI: 10.1021/acs.chemmater.8b01965

enhances electrochemical performance, extending cyclability to 500 cycles with 80% retention of initial capacity.[16] Fe substitution—specifically, aliovalent Fe^{3+} substitution in Li^+ (M1) and transition metal M^{2+} (M2) sites obtained by such simple air-annealing process—has been well-known for other phosphates such as LFP and $LiMn_{1-x}Fe_xPO_4$ (LMFP) to cause changes in the structural characteristics (defective) and in the electrochemical signature (slope).[17−19] In case of LCP, the Fe^{3+} substitution yields structural stabilization at high potential such 4.5 V vs. Li/Li^+ and creation of vacancies in the Li^+ (M1) sites.[16,20] It is reported that these vacancies contribute to increased Li mobility, thus enhancing rate capability.[16,21] Hanafusa et al. demonstrated that Fe^{3+}-substituted LCP can charge and discharge with negligible capacity loss (<5%) over 150 cycles even in conventional EC-based electrolyte.[20] However, achieving such an excellent cyclability in Fe^{3+}-substituted LCP requires restricting the operating voltage range between 3.5 and 5.0 V vs. Li, thus sacrificing capacity contributed by the Fe^{3+}/Fe^{2+} redox below 3.5 V vs. Li. Moreover, the detailed mechanism responsible for improved cyclability, and the role played by the presence of Fe^{3+} within the LCP crystal structure, remains unclear.

This study aims at elucidating the influence of Fe^{3+} substitution on LCP cyclability by focusing on electrode/electrolyte interface. Using LCP nanoparticles (100 nm in average diameter) highly dispersed within multiwalled carbon nanotube (MWCNT) matrix prepared via ultracentrifugation,[22] we have synthesized different LCP-based materials with different Fe^{3+} amounts. Electrochemical characterizations of the synthesized materials give clear evidence of improved electrochemical stability of LCP as well as enhanced rate capability, with Fe^{3+} substitution. Surface analysis using X-ray photoelectron spectroscopy (XPS) and electron energy loss spectroscopy (EELS) suggest that Fe enrichment of the surface of LCP nanoparticles occurs through the oxidation of Fe^{2+} into Fe^{3+} along with the creation of vacancies at Co^{2+} (M2) sites during the synthesis process. The Fe^{3+}-rich phase on the LCP surface enhances the stability of the delithiated phase, preventing oxidative reactions with electrolytes during high-voltage operation. This surface protection persists over 1000 cycles at 0.2 C and 5000 cycles at 1.0 C as long as the electrochemical reduction of Fe^{3+} is avoided by ensuring that the full range of operating voltages lies above the Fe^{3+}/Fe^{2+} redox potential. Additionally, we first demonstrated for LCP or LCFP materials that the vacancies in Co/Fe M2 sites are responsible for the Li^+ diffusivity enhancement within LCFP crystals and thus for the improvements of C-rate capability. Our findings may offer new approaches for stabilizing the structure of LCP and other high-voltage positive electrodes for use in 5 V-class Li-ion batteries.

EXPERIMENTAL SECTION

Materials. $Co(CH_3COO)_2{\cdot}4H_2O$ (>99%, Wako Pure Chemicals), $Fe(CH_3COO)_2$ (>99%, Sigma-Aldrich Corp.), CH_3COOLi (>98.0%, Wako Pure Chemicals), and H_3PO_4 (>85.0%, Wako Pure Chemicals) were used to prepare $LiCo_{0.8}Fe_{0.2}PO_4$ (LCFP). Citric acid ($C_6H_8O_7$) (>99.5%, Sigma-Aldrich Corp.) was used as a chelating agent. Multiwalled carbon nanotubes (MWCNTs) with a specific surface area of 240 $m^2\ g^{-1}$[23] were used for the preparation of carbon composite. Distilled water (17 MΩ cm) was used as a medium for the entire preparation scheme.

Preparation of $LiCo_{0.8}Fe_{0.2}PO_4$/MWCNT Composite under UC Treatment. First, two kinds of solution (solution A and B) were prepared. Solution A was composed of 0.4000 g of MWCNT and 0.6714 g of H_3PO_4 (1.0 equiv) mixed in 50 mL of ultrapure water under ultrasonication. Solution B was composed of 1.1725 g of $Co(CH_3COO)_2{\cdot}4H_2O$ (0.8 equiv), 0.2027 g of $Fe(CH_3COO)_2$ (0.2 equiv), 0.3922 g of CH_3COOLi (1.0 equiv), and 1.1247 g of citric acid (1.0 equiv) dissolved in 20 mL of ultrapure water. Solution A was subjected to the ultracentrifugation (uc) treatment[22] at 80°C for 5 min before and after the addition of solution B. The uc-treated sol was further dried at 130°C under vacuum for 12 h. The obtained powder made of LCFP precursor and MWCNT was preannealed at 350°C in air for 1 h to remove absorbed water and citric-acid-derived amorphous carbon, then left to cool to room temperature (RT). The preannealed powder was then fast annealed at 650°C under N_2 flow (RT to 650°C in 3 min, dwell for 5 min, 20 min to cooling to RT) to form the LCFP/MWCNT composite (pristine LCFP/MWCNT). The pristine LCFP/MWCNT composite was further annealed at 350°C for 3 h under air in order to oxidize Fe^{2+} into Fe^{3+} without incinerating MWCNTs (air-annealed LCFP/MWCNT).

Physicochemical Characterization of $LiCo_{0.8}Fe_{0.2}PO_4$/MWCNT Composite. Structure analysis on pristine and air-annealed LCFP samples was performed by X-ray diffraction [XRD, Smart-lab (Rigaku), Cu Kα radiation (λ = 1.54 Å), operating at 45 kV, 200 mA]. XRD patterns were recorded in the 10°−90° 2θ range at a scan speed of 0.0033° s^{-1}. Time-of-flight neutron powder diffraction (NPD) measurements were performed at the iMATERIA (BL20) facility of the Japan Photon Accelerator Research Complex (J-PARC, Ibaraki, Japan) to obtain NPD patterns corresponding to 0.5−4.8 Å in d-spacing. ^{57}Fe Mössbauer spectra were collected at room temperature in transmission geometry on a constant acceleration spectrometer using a ^{57}Co source in a Rh matrix. Isomer shift (IS) calibrations were performed using α-Fe as a standard at room temperature. The obtained spectrum was fitted by two Lorentzian doublets (Fe^{2+} and Fe^{3+}). The LCFP/MWCNT nanostructure and the particle size were characterized by high-resolution transmission electron microscopy (HRTEM, Hitachi model H9500). Thermogravimetric analysis was performed under a synthetic air (O_2: 20%, N_2: 80%) using a thermogravimetric/differential thermal analyzer (TG/DTA, Seiko Instruments TG/DTA6300). X-ray photoelectron spectroscopy (XPS JEOL Ltd. JPS-9200) was carried out using Mg X-ray source. Prior to the XPS characterization, the sample electrodes were thoroughly washed by dimethyl carbonate (DMC) and dried overnight. X-ray adsorption fine structure (XAFS) measurements at the Co and Fe K-edges for the composite were performed in transmission mode at the beamline BL01 of the synchrotron radiation facility SPring-8 (Hyogo, Japan). Laminate-type two-electrode cells (pouch cells) were assembled using lithium metal foil as a negative electrode and $LiCo_{0.8}Fe_{0.2}PO_4$/MWCNT composite as a positive electrode. The obtained XAFS spectra were analyzed using the spectral fitting software REX2000 (Rigaku Corp.) to evaluate the ratio of Co and Fe species using references selected to exhibit different oxidation states, such as Co^{2+} ($LiCoPO_4$ bulk sample), Co^{3+} (Cobalt acetylacetonate), Fe^{2+} ($LiFePO_4$ bulk sample), and Fe^{3+} ($FePO_4$ bulk sample oxidized by the chemical method using NO_2BF_4).

Electrochemical Characterization of $LiCo_{0.8}Fe_{0.2}PO_4$/MWCNT Composite. Half-cells were assembled using a negative Li metal electrode and a positive $LiCo_{0.8}Fe_{0.2}PO_4$/MWCNT electrode in 2032 coin-type cells. The electrolyte was a mixture of ethylene carbonate, propyl carbonate, and dimethyl carbonate (EC: PC: DMC = 1:1:3) containing 1.0 M of lithium hexafluorophosphate ($LiPF_6$). $LiCo_{0.8}Fe_{0.2}PO_4$/MWCNT electrode was prepared by mixing 90 wt % of the composite and 10 wt % of polyvinylidene difluoride (PVdF) in N-methyl pyrrolidone (NMP). The mixture was coated on an etched-Al foil (current collector) and dried at 80°C in vacuum for 12 h. The loading mass of the composite was 1.4 mg cm^{-2} on etched Al current collector (1.54 cm^2). Charge−discharge tests were performed in constant-current constant-voltage mode between 2.5 and 5.0 V or 4.3 and 5.0 V vs. Li/Li^+ at current density of 0.2 C-rate except the 1st where 0.1 C-rate current was applied as pre-conditioning, assuming that 1C-rate equals 167 mA g^{-1}. The cutoff current density at the constant-voltage mode was 8.35 mA g^{-1} (0.05 C).

Table 1. Rietveld Refinement Results of Neutron Powder Diffraction Patterns for Air-Annealed LCFP/MWCNT Composite[a]

space group		a/Å		b/Å	c/Å		v/Å^3
Pnma		10.1592(7)		5.9114(4)	4.7091(3)		282.80(3)
	atom	Wyckoff	x/a	y/b	z/c	B_{ISO}	occupancy
M1 site	Li^+	4a	0	0	0	2.6(2)	0.984(7)
(Li site)	Fe^{3+}	4a	0	0	0	2.6(2)	0.024(1)
M2 site	Co^{2+}	4c	0.2763(2)	0.25	0.9892(4)	1.19(5)	0.762(2)
(Co site)	Fe^{3+}	4c	0.2763(2)	0.25	0.9892(4)	1.19(5)	0.129(2)
	P	4c	0.0925(2)	0.25	0.4200(2)	0.89(2)	1
	O^-	4c	0.10209(9)	0.25	0.7443(2)	0.84(2)	1
	O^-	4c	0.45393(9)	0.25	0.1982(2)	1.13(2)	1
	O^-	8d	0.16820(8)	0.0466(2)	0.2817(2)	1.09(2)	1

[a] R_{wp} = 5.76, R_p = 4.49, R_e = 2.34, X^2 = 6.07

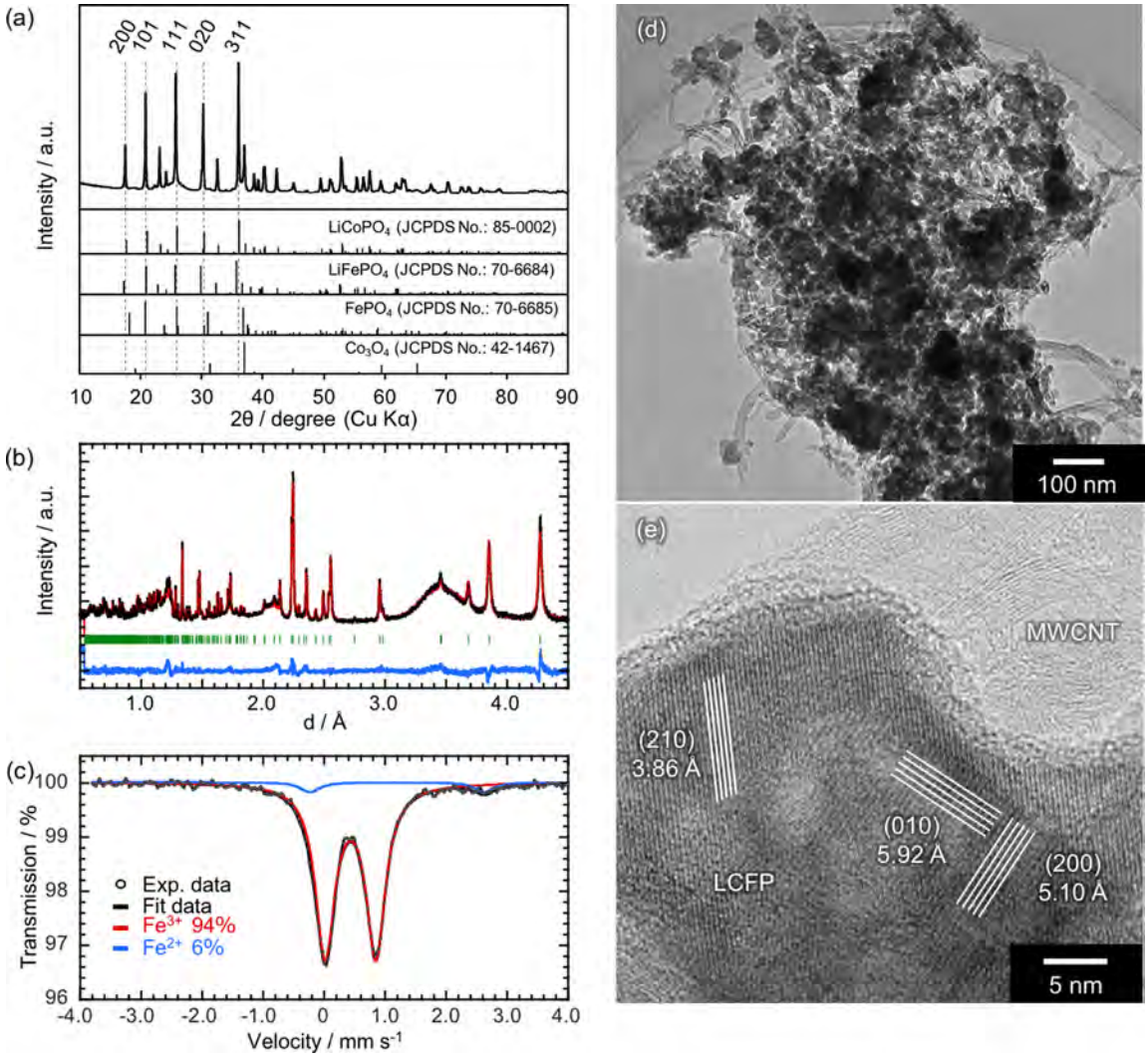

Figure 1. Structural characterization of air-annealed $LiCo_{0.8}Fe_{0.2}PO_4$ (LCFP)/ MWCNT composite. (a) XRD patterns and (b) neutron powder diffraction patterns for air-annealed LCFP/MWCNT composite. (c) Mössbauer spectrum fitted with two Fe environments (Fe^{2+} and Fe^{3+}). (d) Lower-magnification (20 000×) higher-resolution TEM image for highly dispersed LCFP nanocrystalline within the MWCNT matrix. (e) Magnified (400 000×) HRTEM image of the LCFP nanocrystalline. Clear lattice fringes of d = 3.86, 5.10, and 5.92 Å appear, corresponding to the (210), (200), and (010) planes of LCFP, respectively.

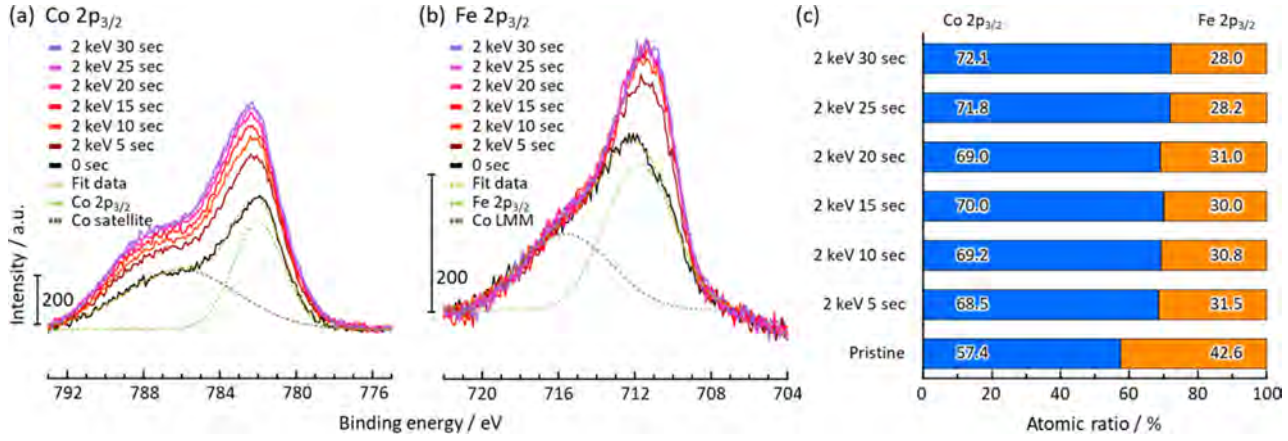

Figure 2. Consecutive XPS measurements with data acquisition at 5 s intervals during 0−30 s Ar ion etching, yielding a depth profile of air-annealed LCFP/MWCNT composite: (a) Co $2p_{3/2}$ peak and Co satellite peak, (b) Fe $2p_{3/2}$ peak and Co LMM Auger electron peak, (c) atomic ratio of Co and Fe calculated from Co $2p_{3/2}$ and Fe $2p_{3/2}$ peaks.

RESULTS AND DISCUSSION

Figure 1a shows the X-ray diffraction pattern of the synthesized air-annealed $LiCo_{0.8}Fe_{0.2}PO_4$ (LCFP)/multiwalled carbon nanotube (MWCNT) composite. Main peaks of the air-annealed LCFP composite can be indexed with an olivine structure (S.G. *Pnma* $LiCoPO_4$: JCPDS card no. 85-0002). Apart peaks attributed to MWCNT and Co_3O_4 with very small intensity, no other peaks due to possible impurities such as Fe_2O_3, $LiFePO_4$ and $FePO_4$ were detected, indicating successful substitution of Fe into the $LiCoPO_4$ (LCP) crystalline structure. Neutron powder diffraction (NPD) analysis of the air-annealed LCFP (Figure 1b) confirmed the existence of vacancies in the synthesized crystal structure. Lattice parameters, atomic positions, and occupancies, including Li and expected vacancy sites, for air-annealed LCFP were determined through Rietveld refinements on the NPD data. The observed NPD peaks can be indexed by an olivine structure with lattice constants of a = 10.1592(7) Å, b = 5.9114(4) Å, and c = 4.7091(3) Å and a unit-cell volume of V = 282.80(3) Å^3, as shown in Table 1. These values of the a and b lattice parameters and the cell volume are smaller than those of $LiCoPO_4$ (LCP, see Table S1), in good agreement with previous reports.[20] The obtained stoichiometry of the air-annealed LCFP crystal structure is $(Li_{0.98}Fe_{0.02})_{M1}(Co_{0.76}Fe_{0.13}\square_{0.11})_{M2}PO_4$, where M1, M2, and □, respectively, represent Li, Co, and vacancy sites. Fe^{3+} is present primarily at transition metal sites (M2), whereupon vacancies are present at the same M2 site to compensate the valence, unlike previous reports which suggests the creation of vacancies in Li (M1) sites.[16,21] One has to note that vacancies appear overestimated as the composition $(Li_{0.98}Fe_{0.02})_{M1}(Co_{0.785}Fe_{0.13}\square_{0.085})_{M2}PO_4$, is expected to ensure charge compensation. However, this result is related to the evidence of the inhomogeneous composition of the particles as described latter. Results of Mössbauer spectroscopy for air-annealed LCFP support the NPD analysis. The obtained spectrum was best fitted by two doublets: one with an isomer shift (IS) = 0.43 mm s^{-1} and a quadrupole splitting (QS) = 0.83 mm s^{-1}, and the other with IS = 1.2 mm s^{-1} and QS = 2.9 mm s^{-1}. The former, accounting for 94% of the absorption area, corresponds to the Fe^{3+} present on M1 and disordered M2 sites,[17,18] and the latter, accounting for 6% of the spectra, corresponds to Fe^{2+} on M2 sites. The high ratio of Fe^{3+} to Fe^{2+} is due primarily to the oxidation of Fe^{2+} in pristine LCFP through the air-annealing process, as pristine LCFP contains only 12% Fe^{3+} (88% Fe^{2+}), as confirmed by the additional Mössbauer spectrum shown in Figure S2b. Most of the Fe^{3+} oxidized from Fe^{2+} was found to remain on the M2 site including also all created vacancies thus leading to highly distorted octahedral surrounding. HRTEM observations of air-annealed LCFP indicate the presence of nanocrystals of ca. 100 nm highly dispersed within the MWCNT matrix (Figure 1d). The high magnification HRTEM image (Figure 1e) shows a highly crystalline bulk part of LCFP nanocrystal surrounded by an amorphous phase. The crystalline bulk part shows clear lattice fringes with interplanar lattice distances of 3.86, 5.10, and 5.92 Å, corresponding respectively to the (210), (200), and (010) planes of the olivine structure.

X-ray photoelectron spectroscopy (XPS) analysis of Co $2p_{3/2}$ and Fe $2p_{3/2}$ energy levels was performed on air-annealed LCFP (Figure 2a,b) subjected to different Ar ion etching duration. The Co/Fe ratio was determined quantitatively by computing the areas under the Co $2p_{3/2}$ and Fe $2p_{3/2}$ peaks (Figure 2c). The examination of the results shows that the distribution of Fe and Co varies from the surface to the bulk of the particles. While an average Co/Fe ratio of 83/17 is calculated from NDP refinement, the XPS experiments show that at the surface (no Ar ion etching) this ratio is equal to 57.4/42.6 and progressively increases when moving toward the center of the particle (increasing Ar ion etching duration). In contrast, the Co/Fe ratio of pristine LCFP/MWCNT composite remains fixed at approximately 80/20 independent of location between surface and center of the particle (independent of Ar ion etching duration) (Figure S2). This suggests that the air-annealing process induces, beside the oxidation of the Fe and creation of Co vacancies to balance the charge, the migration of Fe^{3+} ions toward the surface of the particles in the amorphous domain. Such phenomenon is confirmed by the analysis of air-annealed samples of a composite with higher Fe concentration, namely, $LiCo_{0.5}Fe_{0.5}PO_4$/MWCNT. Elemental mapping (Figure S4a) and line analysis (Figure S4c) of this sample confirms the existence of a Fe-rich surface layer on the nanoparticle surface, while the elemental mapping of the pristine $LiCo_{0.5}Fe_{0.5}PO_4$ shows uniform distribution of Fe, Co, O, and P within the particle (Figure S4b). This inhomogeneous distribution of Fe allows, in addition, interpreting the apparently overestimated

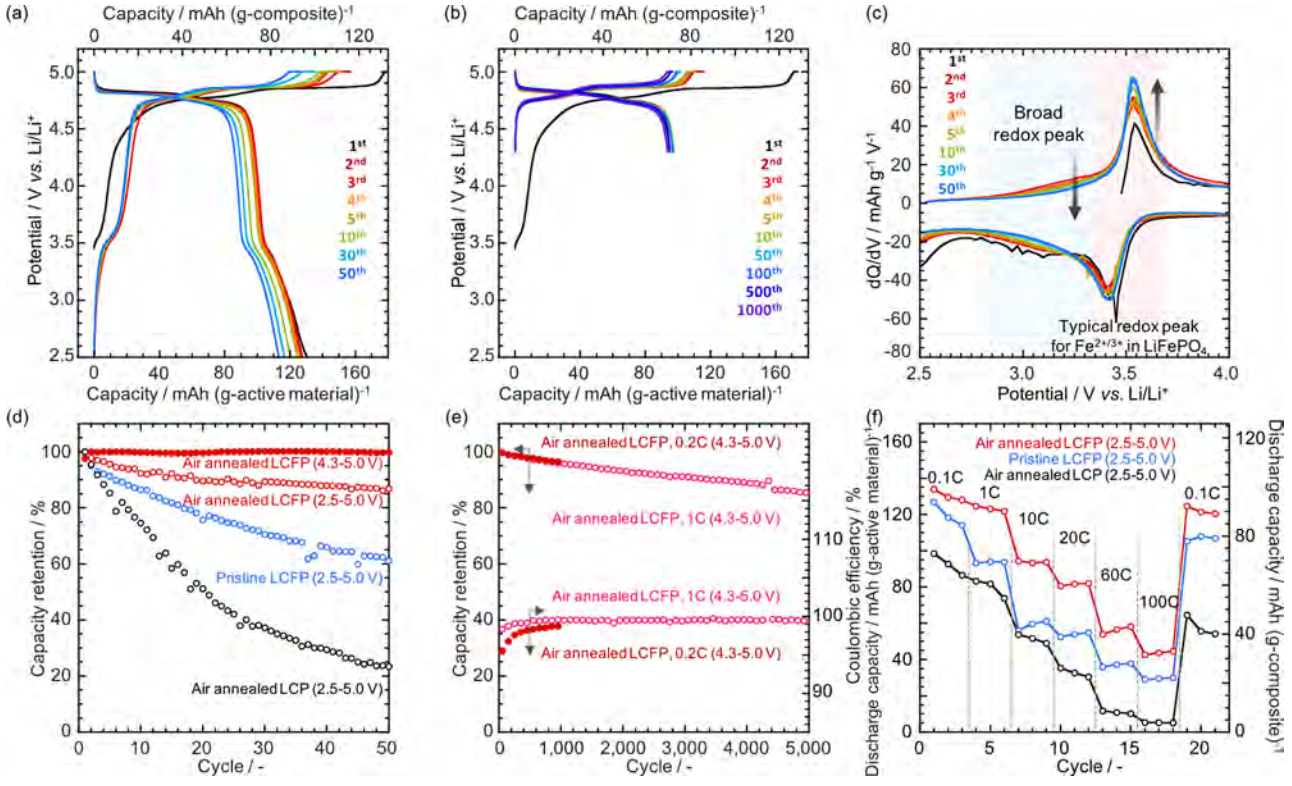

Figure 3. (a) Constant-current charge/discharge curves of a half-cell consisting of Li/1 M $LiPF_6$ EC:PC:DMC(vol. 1:1:3)/(air-annealed LCFP/MWCNT composite) at a 0.2C rate between 2.5 and 5.0 V. (b) Constant-current charge/discharge curves of a half-cell consisting of Li/1 M $LiPF_6$ EC:PC:DMC(vol. 1:1:3)/(air-annealed LCFP/MWCNT composite) at a 0.2C rate between 4.3 and 5.0 V. (c) dQ/dV plot for air-annealed LCFP/MWCNT composite from panel a. (d) Cycle performance for the composites at a 0.2C rate. (e) Cycle performances for the air-annealed LCFP/MWCNT composites of panel b. (f) Rate performance for the composites over the range 2.5−5.0 V.

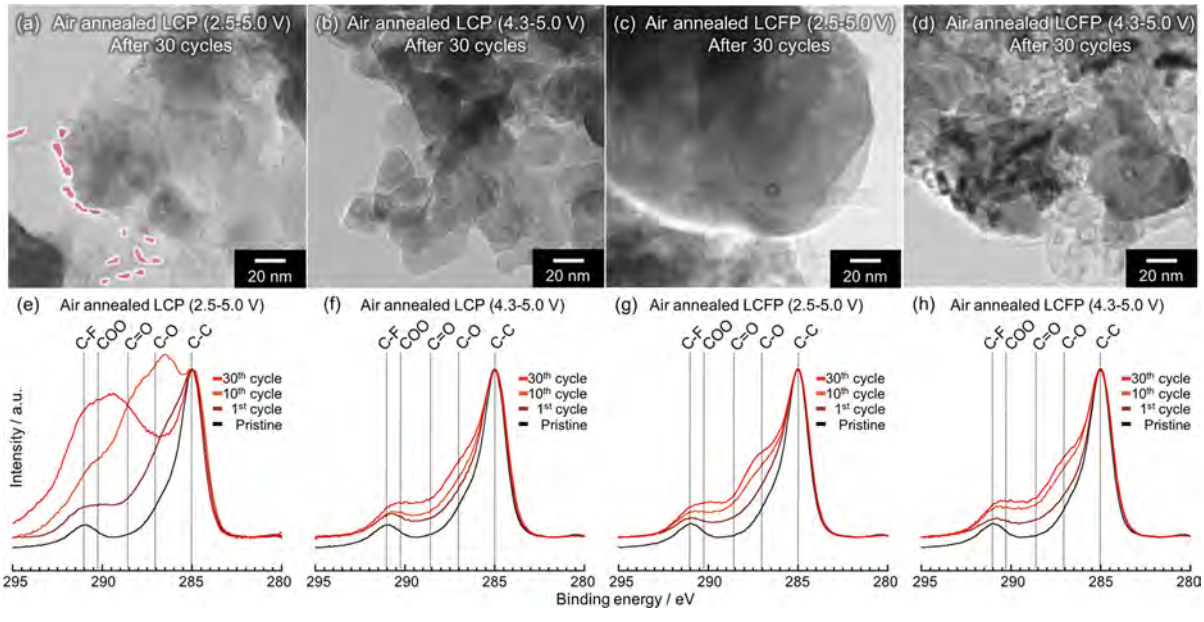

Figure 4. Higher-resolution TEM images of air annealed (a), (b) LCP/MWCNT and (c), (d) LCFP/MWCNT composites after 30 cycles. XPS measurements of air annealed (e)(f) LCP/MWCNT and (g)(h) LCFP/MWCNT composites after 1, 10, and 30 cycles. (a), (c), (e), and (g) are conducted in potential range between 2.5 and 5.0 V. (b), (d), (f), and (h) are conducted in potential range between 4.3 and 5.0 V.

vacancy amount as deduced from the NDP analysis. The migration of Fe^{3+} is associated with equivalent migration of vacancies in the opposite ways leading to an excess of vacancies in the bulk part of the particle and an excess of Fe at the surface. As this surface is amorphous, as revealed by HRTEM, the refinement of NDP take to account only the vacancy-rich part of the particle thus explaining the apparent over-estimation.

The electrochemical behavior of LCFP/MWCNT composites was investigated in half-cells versus Li anode at a rate of

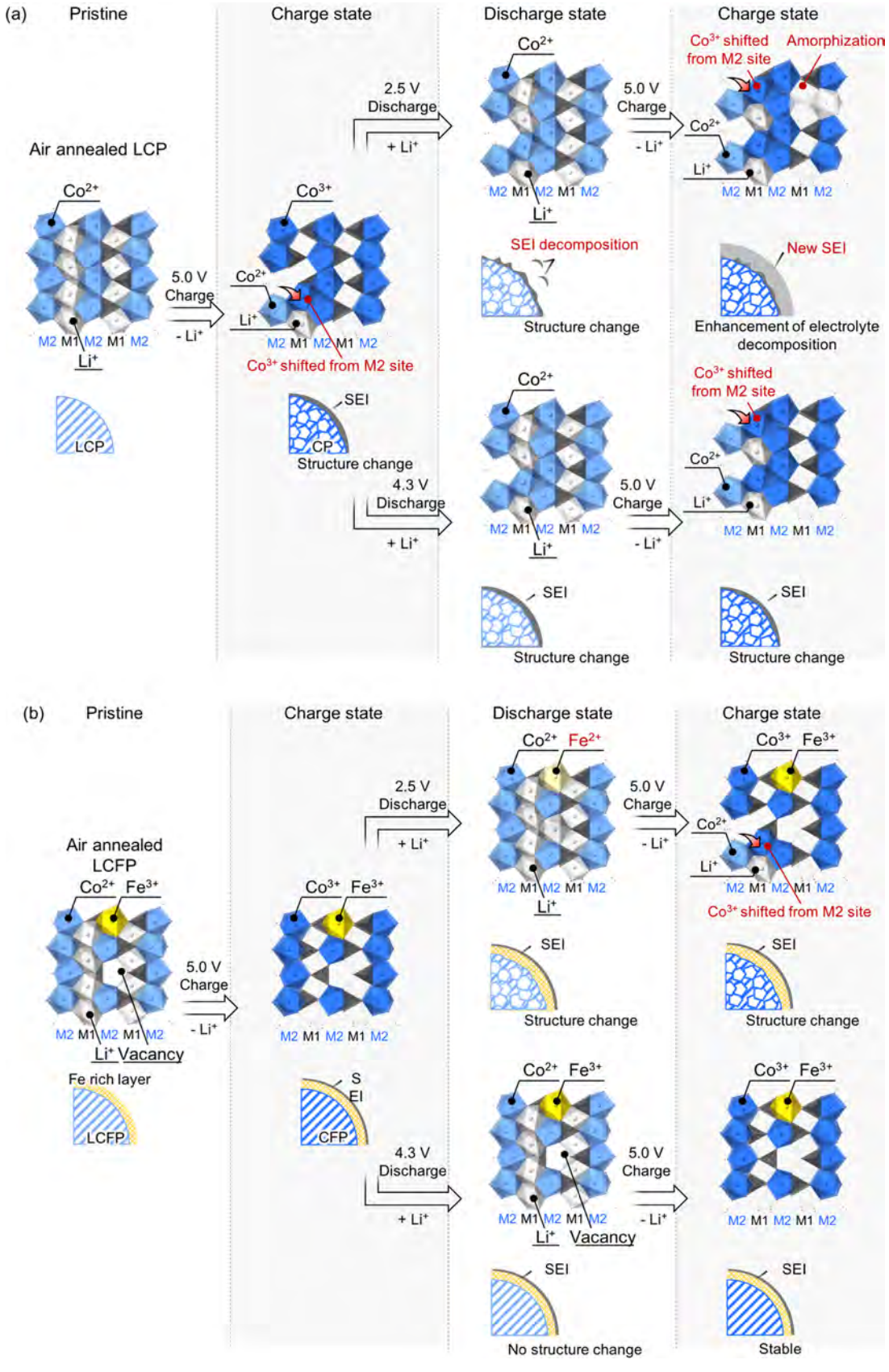

Figure 5. Structural changes of synthesized (a) LCP and (b) LCFP during charge and discharge.

0.2C (1C = 167 mA g^{-1}) (Figure 3). During the charge/discharge processes, a voltage shoulder around 3.5 V and two plateaus were observed at 4.76 and 4.83 V (Figure 3a). The shoulder corresponds to the redox reaction of Fe^{2+}/Fe^{3+} in $LiCo_{0.8}Fe_{0.2}PO_4$. The two plateaus at high potentials correspond to a two-step redox reaction of Co^{2+}/Co^{3+} in

$Li_{0.8}Co_{0.8}Fe_{0.2}PO_4$, which well agrees with previous reports.[20,24,25] The air-annealed LCFP/MWCNT composites showed a high initial discharge capacity of 130 mAh g^{-1} (Figure 3a) and increased stability of the cycle performance with 86% capacity retention after 50 cycles compared to LCP/MWCNT and pristine LCFP/MWCNT composites (Figure 3d). During cycling between 2.5 and 5.0 V, dQ/dV plots show an increase near the Fe^{2+}/Fe^{3+} redox peak at 3.5 V and a decrease near the broad redox peak at 3.4 V (Figure 3c). Such change in redox peaks suggests that Fe^{3+} in the air-annealed LCFP is gradually reduced into Fe^{2+} at low potentials and that the energy level of resultant Fe^{3+} produced by reoxidation of Fe^{2+} is different from that for Fe^{3+} originally existed in the air-annealed LCFP. To avoid this phenomenon, we perform charge and discharge tests of the composites with operating voltages confined to the range 4.3−5.0 V. This results in excellent cycle performance, with 99% capacity retention at 0.2C after 1000 cycles, and 85% at 1C after 5000 cycles (Figure 3e) largely exceeding the best reported one by Hanafusa et al.[20]

Additionally, air-annealed LCFP/MWCNT composite enabled discharge at a 100C rate with capacity of 45 mAh g^{-1}, larger than observed for LCP/MWCNT and pristine LCFP/MWCNT composites (Figure 3f). Comparison of Li^+ diffusion coefficients (D_{Li+}) between the pristine (Fe^{2+}) and air-annealed LCFP (Fe^{3+}) composites shown in Figure S5 supports such improvement in C-rate capability. The obtained D_{Li+} for the air-annealed LCFP is higher in both charge and discharge compared to the pristine. Such results indicate that the creation of vacancies in M2 sites resulting from the oxidation/migration of Fe ions enhances the Li^+ diffusivity within LCFP crystal, unlike previous reports which suggest the enhancement of Li^+ mobility due to the vacancies in Li (M1) sites.[16,21] EIS analysis using symmetric cells[26] (see Figure S6) shows that the pristine LCFP shows higher impedance behavior than air-annealed LCFP (with Fe^{3+}-rich surface). Both the charge transfer and mass transport processes were improved for Fe^{3+}-rich LCFP: the relevant absolute impedance becomes roughly 1/10 for the charge transfer process and 1/5 for the diffusion process when moving from pristine LCFP to air-annealed LCFP.

HRTEM observation and X-ray photoelectron spectroscopy (XPS) analysis of the C 1s energy level were performed on air-annealed LCP/MWCNT and LCFP/MWCNT composites during cycling to confirm the electrochemical behavior (Figure 4). HRTEM images of air-annealed iron-free LCP/MWCNT composites after 30 cycles between 2.5 and 5.0 V showed amorphization of LCP nanocrystals and SEI production on the surface of LCP nanocrystals and MWCNTs (Figure 4a). XPS measurements show an increase of the peak intensity for carboxyl, carbonyl and alkoxy groups (Figure 4 e) which evidence the decomposition of the electrolyte. This suggests that these degradations were caused by unstable $CoPO_4$, which reacts readily with electrolyte. Normally, a stable SEI produced during charge (oxidation) should protect such $CoPO_4$ from reacting with electrolyte. However, SEI decomposition might occur during discharge from 5.0 to 2.5 V. Then, exposed $CoPO_4$ may degrade by reaction with electrolyte, yielding new SEI upon subsequent charging back to 5.0 V. This new SEI obstructs the Li insertion/deinsertion and increases the resistivity. To prevent this, we restrict the voltage range to 4.3−5.0 V to ensure protection of the SEI. The clear difference can be seen both in TEM images and XPS spectra, as neither SEI production nor LCP amorphization are observed after several cycles in the [4.3 V-5.0 V] voltage range (Figure 4b,f). In contrast, air-annealed LCFP/MWCNT composite, exhibits no electrolyte decomposition even upon cycling between 2.5 and 5.0 V (Figure 4c, d, g and h) which confirms that the Fe-rich surface layer contributes to stabilize the delithiated ($Co_{0.8}Fe_{0.2}PO_4$) structure and prevent for electrolyte decomposition. Despite that, cycling the air-annealed LCFP/MWCNT composite between 2.5 and 5.0 V still results in decreasing capacity indicating the existence of another process. This phenomenon is similar to reported one by Paolella et al., who reported a progressive capacity decay for $LiFePO_4$ due to the mixing of Fe and Li cations as deduced from cell parameters evolution.[27] Also, the cell volume deduced from lattice parameter refinement (Figure S7) increases with increasing number of cycles in agreement with a progressive cation mixing in LCFP crystals. Differently, the refinement of the lattice parameters shows that the cell volume remains constant for the samples cycled in the high potential range to avoid the Fe^{3+}/Fe^{2+} redox couple (Figure S7). These results confirm that in the case of LCFP, the reduction of Fe^{3+} to Fe^{2+} at low voltage is also responsible for the cation mixing.

The evolution of Co and Fe valence state along cycling has been determined by X-ray absorption measurements. The X-ray absorption near edge structure (XANES) spectra of Co and Fe K-edge for air-annealed LCFP/MWCNT composite before cycling and at cut off voltages of the two investigated voltage ranges (2.5−5.0 V and 4.3−5.0 V) are shown in Figure S8, while calculated average oxidation states for Co and Fe are reported in Table S3.

In the air-annealed LCFP/MWCNT composite material before cycling, valence states of Co and Fe are +2.1 and +2.9, respectively, in good agreement with previous Mössbauer spectroscopy results (Figure 1c). During cycling in the (2.5−5.0 V) voltage range, the Fe valence state changes between +2.3 and +3.0 at lower and upper cutoff voltages, respectively, and these values remain stable along cycles. The Co valence state at low cut off voltage is equal to +2.1 and remain stable along cycles while at 5.0 V at the end of the first charge it is equal to +2.8 and progressively decreases along cycles to reach +2.55 at the 30^{th} charged state. During cycling in the (4.3−5.0 V) voltage range, Fe valence state, as expected, increases during the first charge from +2.9 in the sample before cycling up to +3. The valence state of +3 is maintained then whatever the voltage along cycles. For the Co, the valence state is +2.1 and +2.8 at 4.3 and 5.0 V, respectively. These values are stable along cycles. This stable cycle performance confirms the specific role of the Fe^{3+} which together with vacancies at M2 sites of LCFP effectively prevents irreversible changes in crystal structure. This stabilizing effect added to the previously detailed prevention of decomposition of electrolyte during charge and discharge processes, result in stable cycle performance with improved rate performance for Fe-substituted samples.

Based on the results of XRD, neutron diffraction analysis, Mössbauer, XANES, and XPS studies, we propose the schematic picture illustrated by Figure 5 for the structural changes occurring during cycling. Upon cycling, LCP as a reference material suffers both structural degradation (Li−Co cation mixing) and SEI accumulation on the particle surface, while only the latter can be restrained by a high cutoff voltage operation within the range of 4.3 and 5.0 V (Figure 5a). Fe^{3+} was introduced as a partial substitute for Co in our material. It

was observed that, upon air annealing, some of the introduced Fe^{3+} cations migrated to the nanoparticle surface, producing vacancies at M2 sites. However, the vacancies disappeared during cycling between 2.5 and 5.0 V, due to the reduction of Fe^{3+} into Fe^{2+} at 3.5 V, resulting in a destabilization of the charged $Co_{0.8}Fe_{0.2}PO_4$ structure. In contrast, the Fe^{3+} surface-rich structure with vacancies at M2 sites and intact SEI remains stable as long as the charge/discharge potential is confined between 4.3 and 5.0 V to avoid redox reactions of Fe^{2+}/Fe^{3+}. This structure results in stable cycle performance.

CONCLUSIONS

In conclusion, a detailed understanding of the mechanism of LCP structure stabilization by Fe^{3+} substitution suggests that the Fe^{3+}-rich phase formed on the LCP surface plays a significant role in yielding stable charge−discharge performance. The oxidation of Fe^{2+} into Fe^{3+} during air annealing of the pristine LCFP results in diffusion of Fe ions to the surface due to the increased repulsion between Fe^{3+} and Co^{2+}. The Fe^{3+}-rich phase on the surface stabilizes the unstable delithiated phase of $(Li_xFe_{0.02})_{M1}(Co_{0.76}Fe_{0.13}\square_{0.11})_{M2}PO_4$ ($x \ll 1$), preventing both the crystal structure degradation and continuous SEI formation on the LCFP nanoparticle surface. The phase stabilization yields excellent cyclability, with 85% capacity retention over 5000 cycles at 1C and 96% capacity retention over 1000 cycles even at a slow C-rate of 0.2C. The importance of Fe^{3+} retention in the crystal structure, which requires to prevent Fe^{3+} reduction to Fe^{2+} around 3.5 V vs. Li/Li^+, was demonstrated by a combination of XRD and XAFS analysis on samples with and without operation-voltage extending below 3.5 V vs. Li. Meanwhile, differently from previous reports, it was found that the vacancies on Co/Fe M2 sites improve the overall electrochemical performances such as the capacity and C-rate capability, thanks to the enhancement of Li^+ diffusivity within LCFP crystals. By demonstrating the existence of the Fe-rich phase on LCFP nanoparticles and its critical impact on electrochemical performance, this study may open the way to the design of stable 5 V cathode materials via fine-tuning of surface phenomena.

ASSOCIATED CONTENT

Supporting Information

The Supporting Information is available free of charge on the ACS Publications website at DOI: 10.1021/acs.chemmater.8b01965.

Additional experimental data: Neutron powder diffraction, XRD, Mössbauer spectroscopy, XPS, XAFS and elemental mapping line analysis for air-annealed LCP/MWCNT, LCFP/MWCNT and pristine LCFP/MWCNT composites (PDF)

AUTHOR INFORMATION

Corresponding Authors

*E-mail: iwama@cc.tuat.ac.jp.

*E-mail: k-naoi@cc.tuat.ac.jp.

ORCID

Patrice Simon: 0000-0002-0461-8268

Katsuhiko Naoi: 0000-0002-0265-2235

Notes

The authors declare no competing financial interest.

ACKNOWLEDGMENTS

This study was supported by the Global Innovation Research Organization in TUAT. This work was supported by JSPS KAKENHI grant numbers JP17K14920. Time-of-flight neutron powder diffraction measurements were performed at the iMATERIA (BL20) facility of the J-PARC (Proposal No. 2017AM0006). The synchrotron radiation experiments were performed at the BL01 of SPring-8 with the approval of the Japan Synchrotron Radiation Research Institute (JASRI) (Proposal No. 2017A1516). We are grateful to Dr. McMahon Thomas Homer Reid for helpful discussion and proofreading.

REFERENCES

(1) Amine, K.; Yasuda, H.; Yamachi, M. Olivine LiCoPO4 as 4.8 V Electrode Material for Lithium Batteries. *Electrochem. Solid-State Lett.* **2000**, *3*, 178−179.

(2) Kang, Y.-M.; Kim, Y.-I.; Oh, M.-W.; Yin, R.-Z.; Lee, Y.; Han, D.-W.; Kwon, H.-S.; Kim, J. H.; Ramanath, G. Structurally stabilized olivine lithium phosphate cathodes with enhanced electrochemical properties through Fe doping. *Energy Environ. Sci.* **2011**, *4*, 4978−4983.

(3) Mauger, A.; Julien, C. M.; Armand, M.; Goodenough, J. B.; Zaghib, K. Li(Ni,Co)PO4 as cathode materials for lithium batteries: Will the dream come true? *Curr. Opin. Electrochem.* **2017**, *6*, 63−69.

(4) Liu, L.; Zhang, H.; Chen, X.; Fang, L.; Bai, Y.; Liu, R.; Wang, Y. Unique synthesis of sandwiched graphene@(Li0.893Fe0.036)Co-(PO4) nanoparticles as high-performance cathode materials for lithium-ion batteries. *J. Mater. Chem. A* **2015**, *3*, 12320−12327.

(5) Xie, J.; Imanishi, N.; Zhang, T.; Hirano, A.; Takeda, Y.; Yamamoto, O. Li-ion diffusion kinetics in LiCoPO4 thin films deposited on NASICON-type glass ceramic electrolytes by magnetron sputtering. *J. Power Sources* **2009**, *192*, 689−692.

(6) Rui, X.; Zhao, X.; Lu, Z.; Tan, H.; Sim, D.; Hng, H. H.; Yazami, R.; Lim, T. M.; Yan, Q. Olivine-Type Nanosheets for Lithium Ion Battery Cathodes. *ACS Nano* **2013**, *7*, 5637−5646.

(7) Fang, L.; Zhang, H.; Zhang, Y.; Liu, L.; Wang, Y. Design and synthesis of two-dimensional porous Fe-doped LiCoPO4 nano-plates as improved cathode for lithium ion batteries. *J. Power Sources* **2016**, *312*, 101−108.

(8) Allen, J. L.; Thompson, T.; Sakamoto, J.; Becker, C. R.; Jow, T. R.; Wolfenstine, J. Transport properties of LiCoPO4 and Fe-substituted LiCoPO4. *J. Power Sources* **2014**, *254*, 204−208.

(9) Ni, J.; Gao, L.; Lu, L. Carbon coated lithium cobalt phosphate for Li-ion batteries: Comparison of three coating techniques. *J. Power Sources* **2013**, *221*, 35−41.

(10) Doan, T. N. L.; Taniguchi, I. Preparation of LiCoPO4/C nanocomposite cathode of lithium batteries with high rate performance. *J. Power Sources* **2011**, *196*, 5679−5684.

(11) Markevich, E.; Salitra, G.; Fridman, K.; Sharabi, R.; Gershinsky, G.; Garsuch, A.; Semrau, G.; Schmidt, M. A.; Aurbach, D. Fluoroethylene Carbonate as an Important Component in Electrolyte Solutions for High-Voltage Lithium Batteries: Role of Surface Chemistry on the Cathode. *Langmuir* **2014**, *30*, 7414−7424.

(12) Markevich, E.; Sharabi, R.; Gottlieb, H.; Borgel, V.; Fridman, K.; Salitra, G.; Aurbach, D.; Semrau, G.; Schmidt, M. A.; Schall, N.; Bruenig, C. Reasons for capacity fading of LiCoPO4 cathodes in LiPF6 containing electrolyte solutions. *Electrochem. Commun.* **2012**, *15*, 22−25.

(13) Bramnik, N. N.; Nikolowski, K.; Trots, D. M.; Ehrenberg, H. Thermal Stability of LiCoPO4 Cathodes. *Electrochem. Solid-State Lett.* **2008**, *11*, A89−A93.

(14) Ehrenberg, H.; Bramnik, N. N.; Senyshyn, A.; Fuess, H. Crystal and magnetic structures of electrochemically delithiated Li1−xCoPO4 phases. *Solid State Sci.* **2009**, *11*, 18−23.

(15) Sharabi, R.; Markevich, E.; Fridman, K.; Gershinsky, G.; Salitra, G.; Aurbach, D.; Semrau, G.; Schmidt, M. A.; Schall, N.; Bruenig, C. Electrolyte solution for the improved cycling performance of

LiCoPO4/C composite cathodes. *Electrochem. Commun.* **2013**, *28*, 20−23.
(16) Allen, J. L.; Jow, T. R.; Wolfenstine, J. Improved cycle life of Fe-substituted LiCoPO4. *J. Power Sources* **2011**, *196*, 8656−8661.
(17) Amisse, R.; Hamelet, S.; Hanzel, D.; Courty, M.; Dominko, R.; Masquelier, C. Nonstochiometry in LiFe0.5Mn0.5PO4: Structural and Electrochemical Properties. *J. Electrochem. Soc.* **2013**, *160*, A1446−A1450.
(18) Hamelet, S.; Gibot, P.; Casas-Cabanas, M.; Bonnin, D.; Grey, C. P.; Cabana, J.; Leriche, J.-B.; Rodriguez-Carvajal, J.; Courty, M.; Levasseur, S.; Carlach, P.; Van Thournout, M.; Tarascon, J.-M.; Masquelier, C. The effects of moderate thermal treatments under air on LiFePO4-based nano powders. *J. Mater. Chem.* **2009**, *19*, 3979−3991.
(19) Amisse, R.; Sougrati, M. T.; Stievano, L.; Davoisne, C.; Dražič, G.; Budič, B.; Dominko, R.; Masquelier, C. Singular Structural and Electrochemical Properties in Highly Defective LiFePO4 Powders. *Chem. Mater.* **2015**, *27*, 4261−4273.
(20) Hanafusa, R.; Oka, Y.; Nakamura, T. Electrochemical and Magnetic Studies of Li-Deficient Li1-xCo1-xFexPO4 Olivine Cathode Compounds. *J. Electrochem. Soc.* **2015**, *162*, A3045−A3051.
(21) Allen, J. L.; Allen, J. L.; Thompson, T.; Delp, S. A.; Wolfenstine, J.; Jow, T. R. Cr and Si Substituted-LiCo0.9Fe0.1PO4: Structure, full and half Li-ion cell performance. *J. Power Sources* **2016**, *327*, 229−234.
(22) Iwama, E.; Simon, P.; Naoi, K. Ultracentrifugation: An effective novel route to ultrafast nanomaterials for hybrid supercapacitors. *Curr. Opin. Electrochem.* **2017**, *6*, 120.
(23) Iwama, E.; Kawabata, N.; Nishio, N.; Kisu, K.; Miyamoto, J.; Naoi, W.; Rozier, P.; Simon, P.; Naoi, K. Enhanced Electrochemical Performance of Ultracentrifugation-Derived nc-Li3VO4/MWCNT Composites for Hybrid Supercapacitors. *ACS Nano* **2016**, *10*, 5398−5404.
(24) Bramnik, N. N.; Nikolowski, K.; Baehtz, C.; Bramnik, K. G.; Ehrenberg, H. Phase Transitions Occurring upon Lithium Insertion−Extraction of LiCoPO4. *Chem. Mater.* **2007**, *19*, 908−915.
(25) Kaus, M.; Issac, I.; Heinzmann, R.; Doyle, S.; Mangold, S.; Hahn, H.; Chakravadhanula, V. S. K.; Kübel, C.; Ehrenberg, H.; Indris, S. Electrochemical Delithiation/Relithiation of LiCoPO4: A Two-Step Reaction Mechanism Investigated by in Situ X-ray Diffraction, in Situ X-ray Absorption Spectroscopy, and ex Situ 7Li/31P NMR Spectroscopy. *J. Phys. Chem. C* **2014**, *118*, 17279−17290.
(26) Kisu, K.; Aoyagi, S.; Nagatomo, H.; Iwama, E.; Reid, M. T. H.; Naoi, W.; Naoi, K. Internal resistance mapping preparation to optimize electrode thickness and density using symmetric cell for high-performance lithium-ion batteries and capacitors. *J. Power Sources* **2018**, *396*, 207−212.
(27) Paolella, A.; Bertoni, G.; Hovington, P.; Feng, Z.; Flacau, R.; Prato, M.; Colombo, M.; Marras, S.; Manna, L.; Turner, S.; Van Tendeloo, G.; Guerfi, A.; Demopoulos, G. P.; Zaghib, K. Cation exchange mediated elimination of the Fe-antisites in the hydrothermal synthesis of LiFePO4. *Nano Energy* **2015**, *16*, 256−267.

■ NOTE ADDED AFTER ASAP PUBLICATION

This article was published ASAP on September 21, 2018, with errors in Figures 1 and 3−5, Table 1, and in the Supporting Information. The corrected version was reposted on September 27, 2018.

Supporting Information

Stabilizing the structure of $LiCoPO_4$ nanocrystals *via* addition of Fe^{3+}: Formation of Fe^{3+} surface layer, creation of diffusion-enhancing vacancies, and enabling high-voltage battery operation

Naohisa Okita,[1] Kazuaki Kisu,[1, 2] Etsuro Iwama,[*, 1, 2] Yuki Sakai,[1] Yiyo Lim,[1] Yusuke Takami,[1] Moulay Tahar Sougrati, [4, 5] Thierry Brousse,[2, 4, 6] Patrick Rozier,[2, 4, 7] Patrice Simon, [2, 4, 7] Wako Naoi,[8] and Katsuhiko Naoi[*, 1, 2, 3]

[1]*Department of Applied Chemistry,* [2]*Global Innovation Research Organization, and* [3]*Advanced Capacitor Research Center, Tokyo University of Agriculture & Technology, 2-24-16 Naka-cho, Koganei, Tokyo, 184-8588 Japan*
[4]*Réseau sur le Stockage Electrochimique de l'Energie, RS2E FR CNRS 3459*
[5]*Institute Charles Gerhardt Montpellier (ICGM), UMR 5253, Université de Montpellier, CNRS, 34059 Montpellier Cedex 5, France*
[6]*Institut des Matériaux Jean Rouxel (IMN), UMR 6502, Université de Nantes, CNRS, rue Christian Pauc, BP50609, 44306 Nantes Cedex 3, France*
[7]*CIRIMAT, Université de Toulouse, CNRS, INPT, UPS, 118 route de Narbonne 31062 Toulouse cedex 9, France*
[8]*Division of Art and Innovative Technologies, K & W Inc., 1-3-16-901 Higashi, Kunitachi, Tokyo 186-0002, Japan*

[*]E-mail: iwama@cc.tuat.ac.jp / k-naoi@cc.tuat.ac.jp

Neutron powder diffraction analysis on the air-annealed $LiCoPO_4$ (LCP) / Multiwalled carbon nanotube (MWCNT) composite.

To support the structure analysis on the air-annealed $LiCo_{0.8}Fe_{0.2}PO_4$ (LCFP), neutron powder diffraction (NPD) of the air-annealed $LiCoPO_4$ (LCP) was recorded. The synthesis procedure of the air-annealed LCP was as same as described in the main text without an use of Fe species ($Fe(CH_3COO)_2$). Time-of-flight neutron powder diffraction (NPD) measurements were performed at the iMATERIA (BL20) facility of the Japan Photon Accelerator Research Complex (J-PARC, Ibaraki, Japan) to obtain NPD patterns corresponding to 0.5-4.8 Å in d-spacing. Lattice parameters and atomic positions for the air-annealed LCP were determined through Rietveld refinements on the NPD data. The observed NPD peaks shown in Figure S1 can be indexed by an olivine structure with lattice constants of a = 10.2014(1) Å, b = 5.9237(7) Å, and c = 4.7007(5) Å and a unit-cell volume of V =

284.06(5) Å^3, as shown in Table S1. These values of the *a* and *b* lattice parameters and the cell volume are larger than those of LCFP (see Table 1 in the main text). The atomic-position analysis on LCP can be well fitted without vacancies in the synthesized crystal structure unlike the air-annealed LCFP.

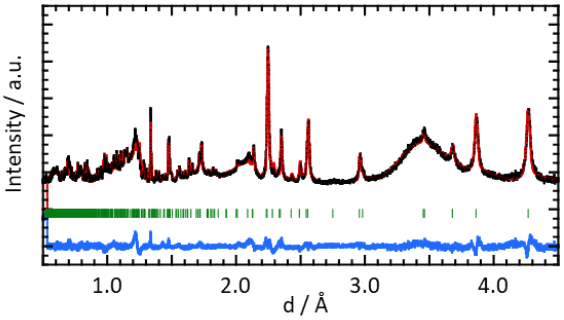

Figure S1 Neutron powder diffraction patterns for the air-annealed LCP / MWCNT composite.

Table S1 Rietveld refinement results of neutron powder diffraction patterns from Figure S1 for the air-annealed LCP / MWCNT composite.

Space group	*a* / Å	*b* / Å	c / Å	*V* / Å^3
Pnma	10.2014(2)	5.9237(7)	4.7007(5)	284.06(5)

	Atom	Wyckoff	*x/a*	*y/b*	*z/c*	B_{iso}	Occupancy
M1 site (Li site)	Li^+	4a	0	0	0	1.01(2)	1.00(1)
M2 site (Co site)	Co^{2+}	4c	0.2775(3)	0.25	0.9781(7)	0.50(7)	1.000(9)
	P	4c	0.0943(2)	0.25	0.4190(3)	0.50(3)	1
	O^-	4c	0.0972(2)	0.25	0.7420(3)	0.50(3)	1
	O^-	4c	0.4543(2)	0.25	0.2037(3)	0.50(3)	1
	O^-	8d	0.1663(1)	0.0430(1)	0.2817(2)	0.50(2)	1

R_{wp} = 5.13, R_p = 3.71, R_e = 1.92, X^2 = 7.14

X-ray diffraction and room temperature Mössbauer spectroscopy on the LCFP/MWCNT with and without the air-annealing process.

Mössbauer spectroscopy was conducted on the pristine LCFP/MWCNT, in order to verify the idea that the air-annealing of the pristine LCFP/MWCNT is the responsible process to create Fe^{3+} in the structure. To begin with, X-ray diffraction (XRD) pattern of the pristine LCFP crystal was recorded. Structure analysis on pristine and air-annealed LCFP samples was performed by X-ray diffraction [XRD, Smart-lab (Rigaku), Cu Kα radiation (λ=1.54 Å), operating at 45 kV, 200 mA]. XRD patterns were recorded in the 10˚- 90˚ 2θ range at a scan speed of 0.0033° s^{-1}. The obtained XRD pattern of the pristine LCFP was shown along with that of the air-annealed LCFP in Figure S2(a). As same as for the air-annealing LCFP, all peaks of both the pristine LCFP composite correspond to a single phase of an olivine structure with *Pnma* space group ($LiCoPO_4$: JCPDS card no. 85-0002). Excluding peaks

attributed to MWCNT, no other peaks due to possible impurities such as Co_3O_4, Fe_2O_3, $LiFePO_4$ and $FePO_4$ were detected, indicating successful substitution of Fe into the $LiCoPO_4$ (LCP) crystalline structure. Lattice parameters for the pristine LCFP were determined through Rietveld refinements on the XRD data, as shown in Table S2. Mössbauer spectroscopy for the pristine LCFP is shown in Figure S2(b) and compared with that for the air-annealing LCFP. ^{57}Fe Mössbauer spectra were collected in transmission geometry on a constant acceleration spectrometer using a ^{57}Co source in a Rh matrix operated at room temperature. Isomer shift (IS) calibrations were performed using a foil α-Fe as a standard at room temperature. The obtained spectrum for the pristine LCFP was best fitted by two Lorentzian doublets: one with isomer shift (IS) = 0.51 mm s^{-1} and quadrupole splitting (QS) = 0.73 mm s^{-1}, and the other with IS = 1.2 mm s^{-1} and QS = 3.0 mm s^{-1}. The former, accounting for 12% of the full spectra, corresponds to the Fe^{3+} present on M1 and disordered M2 sites [1, 2], and the latter, accounting for 88% of the spectra, corresponds to Fe^{2+} on M2 sites. The drastic increase in Fe^{3+} ratio from 12% to 88% indicates that the air-annealing is the main responsible process for the Fe^{3+} creation in the LCFP crystal structure.

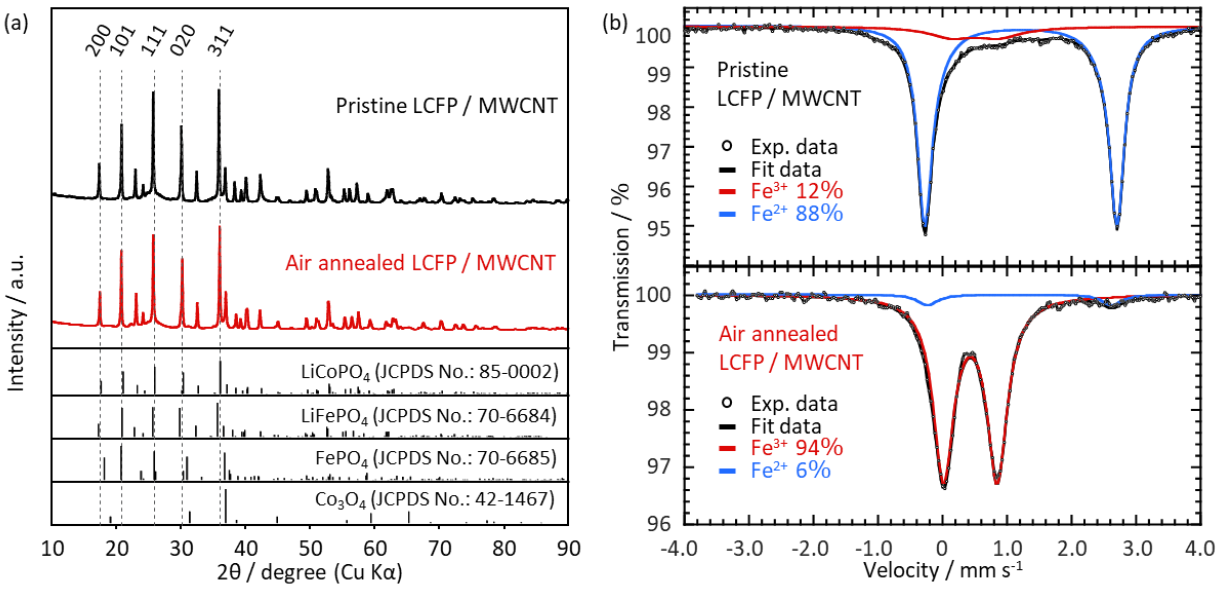

Figure S2 Structural characterization of pristine and the air-annealed LCFP / MWCNT composites. (a) XRD patterns for LCFP /MWCNT composites. (b) Mössbauer spectrum fitted with two Fe environments (Fe^{2+} and Fe^{3+}).

Table S2 Rietveld refinement results of X-ray powder diffraction patterns from Figure S2(a) for pristine and the air-annealed LCFP / MWCNT composite.

	Space group	*a* / Å	*b* / Å	*c* / Å	*V* / Å^3
Pristine LCFP	*Pnma*	10.2237(8)	5.9376(5)	4.6985(4)	285.22(4)
Air annealed LCFP	*Pnma*	10.1589(7)	5.9105(4)	4.7090(3)	282.75(3)

X-ray Photoelectron Spectra of Co $2P_{3/2}$ and Fe $2P_{3/2}$ on the pristine LCFP/MWCNT composite.

The Co/Fe ratio of the pristine LCFP / MWCNT composite was evaluated from the fitting of X-ray photoelectron spectra. X-ray photoelectron spectroscopy (XPS JEOL Ltd. JPS-9200) was carried out with a pass energy of 40 eV for high-resolution scans using a monochromated Mg X-ray source. Prior to the XPS characterization, the sample electrodes were thoroughly washed by dimethyl carbonate (DMC) and dried overnight. The Co/Fe ratio was determined quantitatively by computing the areas under the Co $2p_{3/2}$ and Fe $2p_{3/2}$ peaks (Figure S2). The Co/Fe ratio at the surface of the pristine composite (0 sec) was 80.7/19.3, which well agrees with the dosage of the synthesis process (Co = 0.8 eq and Fe = 0.2 eq, see the paragraph of "Experimental" in the main text). Contrary to the obtained result of the air-annealed LCFP shown in Figure 2, the Fe/Co ratio remains almost fixed, independent of Ar ion etching duration over 30 sec.

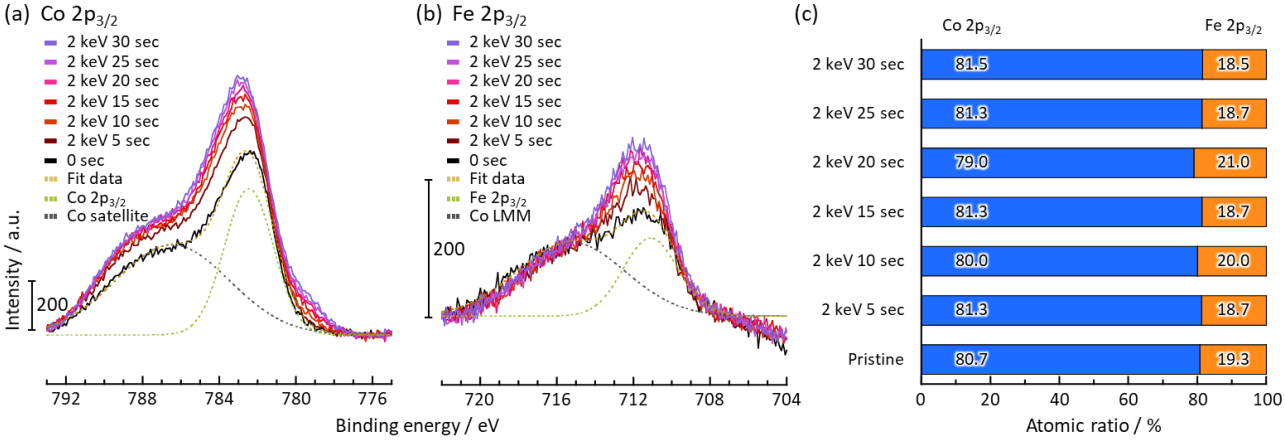

Figure S3 Consecutive XPS measurements with data acquisition at 5 sec intervals during 0–30 sec Ar ion etching, yielding a depth profile of pristine LCFP / MWCNT composite: (a) Co $2p_{3/2}$ peak and Co satellite peak, (b) Fe $2p_{3/2}$ peak and Co LMM Auger electron peak, (c) Atomic ratio of Co and Fe calculated from Co $2p_{3/2}$ and Fe $2p_{3/2}$ peaks.

Electron energy-loss spectroscopy measurements on the pristine and air-annealed LCFP crystals ($LiCo_{0.5}Fe_{0.5}PO_4$ / MWCNT)

To support the hypothesis of an Fe-rich phase on the surface of air-annealed LCFP crystals based on the analysis of XPS spectra (Figure 2 in the main text), we conducted the electron energy-loss spectroscopy on the sample. Here, to compensate for the low ratio of Fe/Co in the composite and the corresponding low intensity of Fe in synthesized LCFP/MWCNT structures, we prepared the pristine and air-annealed samples of a composite with higher Fe concentration, namely $LiCo_{0.5}Fe_{0.5}PO_4$ / MWCNT. As shown in Figure S4(a), elemental mapping of the air-annealed $LiCo_{0.5}Fe_{0.5}PO_4$ /

MWCNT composite shows an Fe-rich surface layer on the nanoparticle surface which is supported by its line analysis [Figure S4(c)], where as that of the pristine in Figure S4(b) shows uniform distribution of Fe, Co, O, and P within the particle.

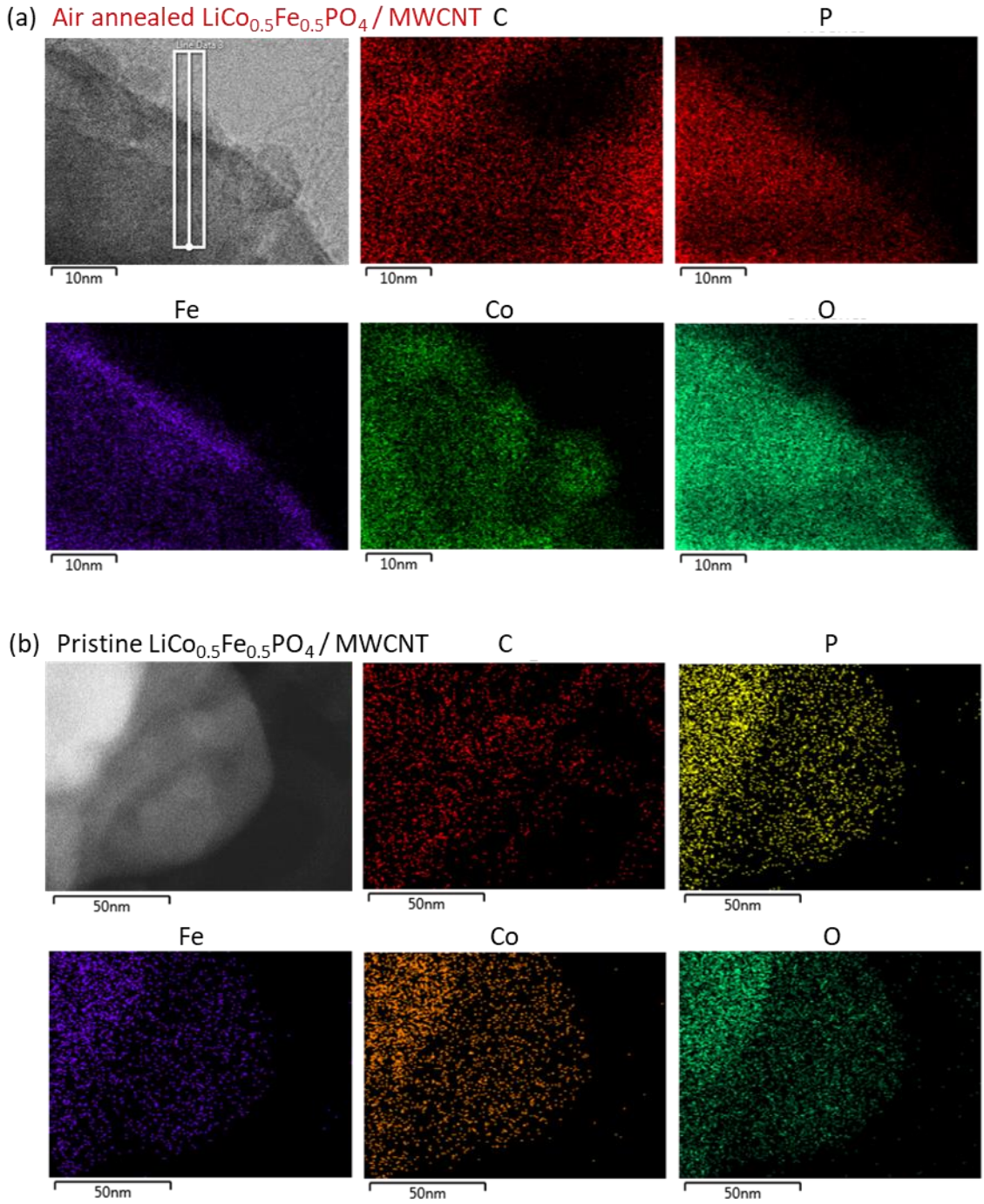

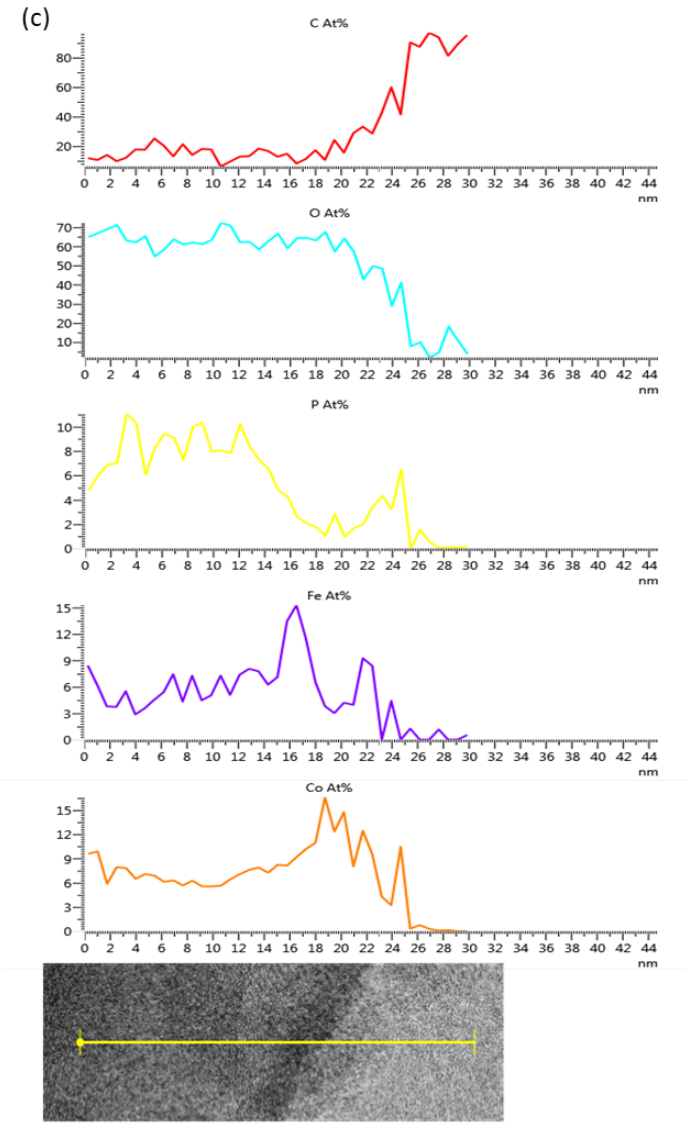

Figure S4 Elemental mapping line analysis of (a)air annealed $LiCo_{0.5}Fe_{0.5}PO_4$ / MWCNT and (b) pristine $LiCo_{0.5}Fe_{0.5}PO_4$ / MWCNT composites, (c)line analysis of the air annealed $LiCo_{0.5}Fe_{0.5}PO_4$ / MWCNT composite [shown in white frame in Figure S4(a)] obtained from electron energy loss spectroscopy.

Enhancement of lithium ion diffusion coefficients (D_{Li+}): galvanostatic intermittent titration technique (GITT) on the pristine and air-annealed LCFP/MWCNT composites.

In order to elucidate the factor for the C-rate capability enhancement as shown in Figure 3(f) of the manuscript, GITT measurements were conducted and calculated D_{Li+} was compared between the pristine (Fe^{2+}) and air-annealed LCFP (Fe^{3+} and resulted vacancies in Co/Fe M2 sites). As shown in Figure S5(a) and S5(b), D_{Li+} for the air-annealed LCFP (Fe^{3+} giving vacancy in Co site) is higher compared to the pristine (Fe^{2+}) especially in the high potential region (high SOC and low SOD), which

is consistent with the results of C-rate capability tests. These results indicate that the existence of vacancies in M2 site enhances the kinetics of LCFP reaction, and the stable SEI mainly contributes to the cycling stability.

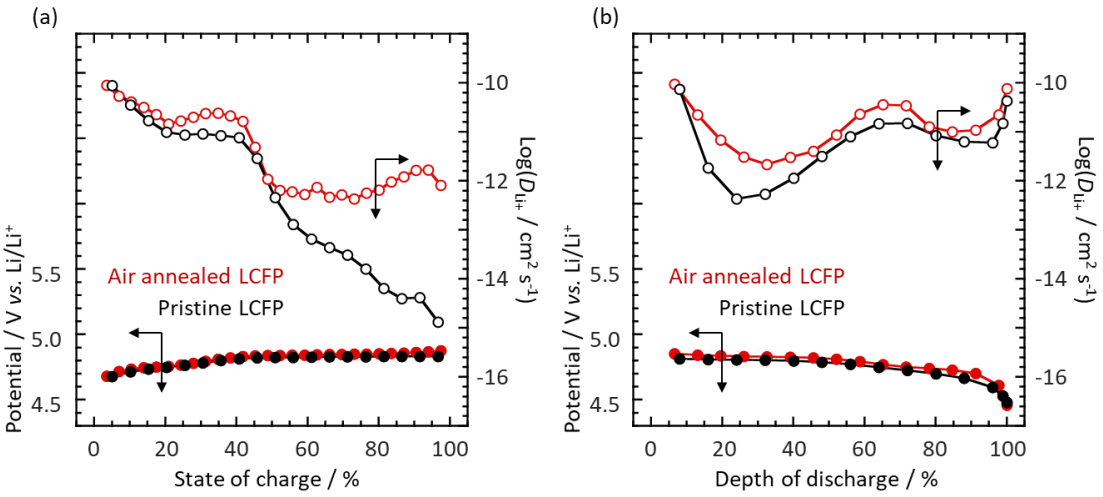

Figure S5. Plots of Li diffusion coefficients *vs.* state of charge/discharge calculated from GITT curves during (a) charge and (b) discharge for the pristine and air-annealed LCFP. GITT was conducted with 0.1C (1C = 167 mAh g^{-1} per active material) for 20 min. and rest time for 1h in the potential range of between 4.3-5.0 V *vs.* Li/Li^+. Before GITT measurements, a pre-cycling was conducted at 0.1C in the same potential range as GITT.

Charge-transfer resistance and lithium ion diffusivity: electrochemical impedance spectroscopy (EIS) on the pristine and air-annealed LCFP/MWCNT composites using symmetric cells.

As shown from GITT measurement (Fig.S5), the apparent D_{Li+} was enhanced for the air-annealed LCFP (with Fe^{3+} rich surface) compared with pristine LCFP. However, GITT analysis generally represents overall diffusion kinetics of active materials, thus, it is hard to distinguish between effects of charge transfer and diffusional properties. We made additional EIS experiments on (a) pristine LCFP and (b) Fe^{3+}-rich-surface LCFP at two different SOCs, namely 0 and 70% (middle range of second plateau as shown in Figure 2b). As shown in the Figure S6, the pristine LCFP shows higher impedance behavior than the air-annealed LCFP (with Fe^{3+} rich surface). Both the charge transfer and mass transport processes have been improved for Fe^{3+}-rich LCFP: the relevant absolute impedance becomes roughly 1/10 for the charge transfer process and 1/5 for the diffusion process when moving from pristine LCFP to air-annealed LCFP.

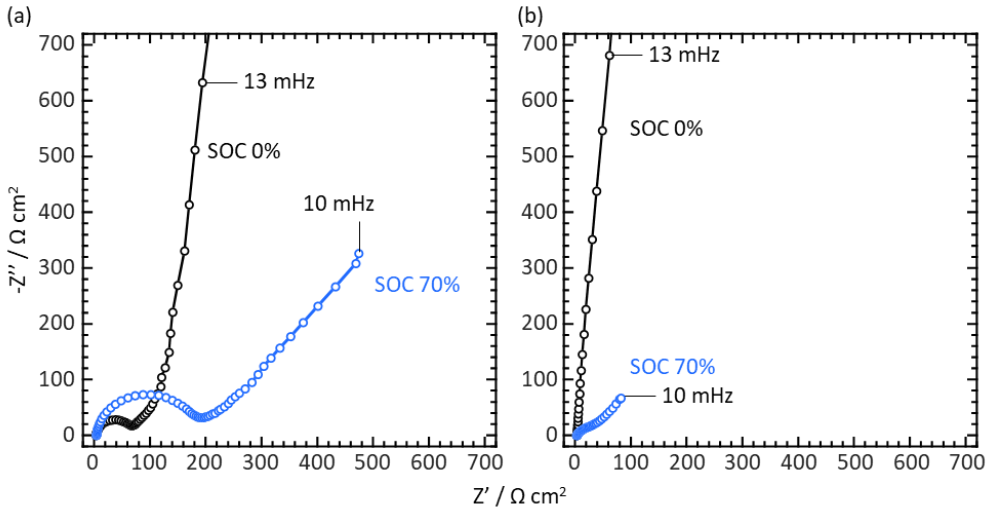

Figure S6 Impedance spectroscopy on (a) pristine LCFP and (b) air-annealed LCFP with Fe^{3+}-rich-surface at two different SOCs, namely, 0 and 70% (middle range of second plateau). The measurement was made on symmetric cells [3] comprising of both LCFP or LCFP (Fe^{3+}-rich) electrodes. Perturbation amplitude was ±10 mV (peak to peak). Frequency ranges was 10 mHz to 65 kHz.

Stability of LCP and LCFP crystal structure at different voltage range operation; 2.5-5.0 V and 4.3-5.0 V (Unit cell volume change).

In order to compare the cycling stability of crystal structure depending on the operation voltage ranges (2.5-5.0 V or 4.3-5.0 V), unit cell volumes for the air-annealed LCFP/MWCNT composites after 1, 10, and 30 cycles were plotted along with those for the air-annealed LCP/MWCNT. Unit cell volumes for the air-annealed LCFP operated within the high voltage range (4.3-5.0 V) remain constant, compared to those for other three samples which show clear increase because of Li-Co mixing during cycling. Such results strongly support the hypothesis that Fe^{3+} and vacancies at M2 sites serve to stabilize the LCFP crystal structure. The air-annealed LCFP operated within 2.5-5.0 V, where its Fe^{3+} undergoes Fe^{3+}/Fe^{2+} redox [see Figure 3 (c) in the main text], cannot resist its initial volume increase. Meanwhile, unit cell volume for the air-annealed LCP continuously increase regardless of its operation voltage range.

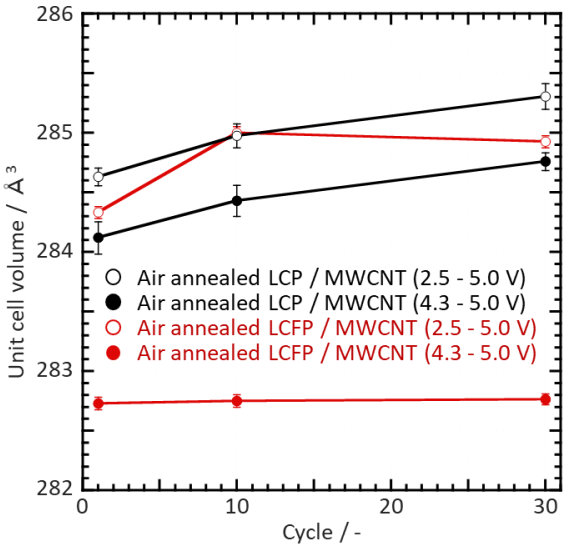

Figure S7 Unit cell volumes of 4 different samples after charge and discharge up to 30 cycles; the air-annealed LCP / MWCNT and air-annealed LCFP / MWCNT composites at 2 different operation voltage ranges (2.5-5.0 V and 4.3-5.0 V). Each unit cell volume was calculated from the cell parameters obtained from corresponding XRD-pattern analysis.

XAFS measurements on air-annealed LCFP/MWCNT composites

To confirm the effect of charge and discharge tests between 4.3 and 5.0 V on air-annealed LCFP/MWCNT composites, redox states of Co and Fe were investigated by X-ray absorption measurements during cycling. The X-ray absorption near edge structure (XANES) spectra of Co and Fe K-edge for air-annealed LCFP / MWCNT composite are shown in Figure S8. The valence state of Co and Fe in the composite is determined by deconvolving the spectra using the contributions of Co^{2+}, Co^{3+}, Fe^{2+} and Fe^{3+}. At 3.45 V, initial valence states of Co and Fe were +2.1 and +2.9, respectively, in good agreement with previous Mössbauer spectroscopy results [Figure 1(c) in the main text]. Valence numbers of Co and Fe during the 1st, 10th and 30th cycles were obtained from the XANES spectra shown in Figure S7 and Table S3. The Fe valence state over charge and discharge cycles between 2.5 and 5.0 V varied from +2.3 to +3.0, accompanied by a corresponding decrease in change of Co valence state. During cycling between 4.3 and 5.0 V, the valence number of Co exhibited minimal variation, ranging from +2.1 to +2.8 over all cycles. This stable cycle performance is made possible by the constancy of the valence state of Fe^{3+} after the 1st, 10th and 30th cycles between 4.3 and 5.0 V.

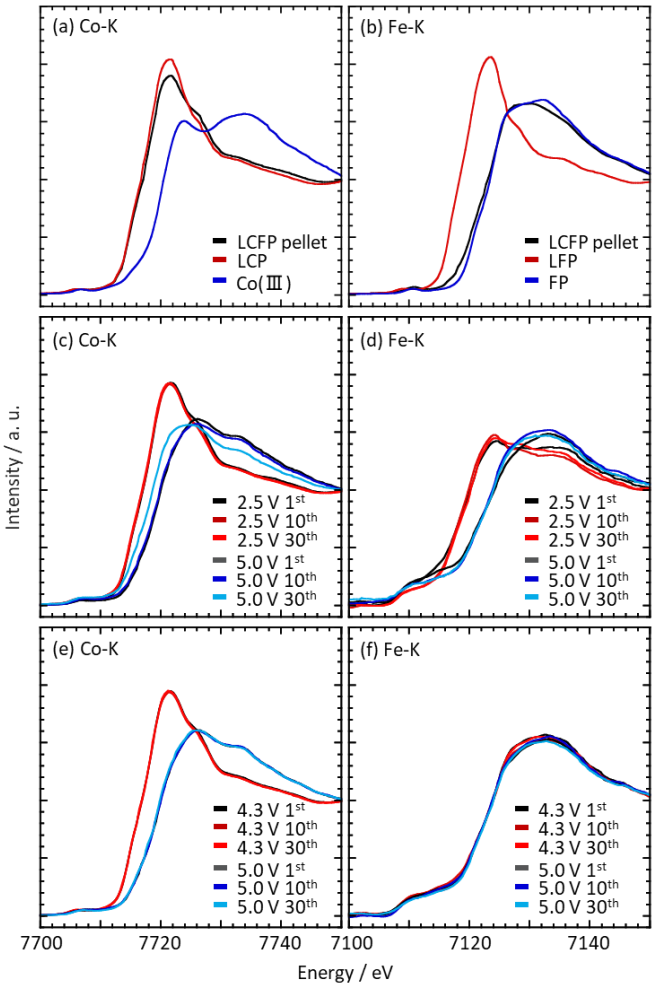

Figure S8 XAFS measurements on a pellet of (a)-(b) air-annealed LCFP / MWCNT composite and (c)-(f) half-cell consisting of Li/1M $LiPF_6$ EC:PC:DMC(vol. 1:1:3)/(air annealed LCFP / MWCNT composite). The XANES spectra at the Co K-edge of the composite are shown in (a), (c) and (e). The XANES spectra at the Fe K-edge of the composite are shown in (b), (d) and (f). (c) and (d) are conducted in potential range between 2.5 and 5.0 V. (e) and (f) are conducted in potential range between 4.3 and 5.0 V.

Table S3 Valence states of Co and Fe of air annealed LCFP / MWCNT composite obtained from XANES spectra shown in Figure S6

		Co valence state		Fe valence state	
	Cycle No.	Discharge	Charge	Discharge	Charge
Before charge/discharge		+2.10		+2.91	
2.5-5.0 V	1st	+2.12	+2.82	+2.33	+3.01
	10th	+2.11	+2.78	+2.27	+3.00
	30th	+2.08	+2.55	+2.36	+3.02
4.3-5.0 V	1st	+2.11	+2.82	+3.02	+3.02
	10th	+2.11	+2.82	+3.01	+3.02
	30th	+2.09	+2.80	+3.01	+3.02

1. Amisse, R.; Hamelet, S.; Hanzel, D.; Courty, M.; Dominko, R.; Masquelier, C., Nonstochiometry in $LiFe_{0.5}Mn_{0.5}PO_4$: Structural and Electrochemical Properties. *J. Electrochem. Soc.* **2013,** 160, A1446-A1450.

2. Hamelet, S.; Gibot, P.; Casas-Cabanas, M.; Bonnin, D.; Grey, C. P.; Cabana, J.; Leriche, J.-B.; Rodriguez-Carvajal, J.; Courty, M.; Levasseur, S.; Carlach, P.; Van Thournout, M.; Tarascon, J.-M.; Masquelier, C., The effects of moderate thermal treatments under air on $LiFePO_4$-based nano powders. *J. Mater. Chem.* **2009,** 19, 3979-3991.

3. Kisu, K.; Aoyagi, S.; Nagatomo, H.; Iwama, E.; Reid, M. T. H.; Naoi, W.; Naoi, K., Internal resistance mapping preparation to optimize electrode thickness and density using symmetric cell for high-performance lithium-ion batteries and capacitors. *J. Power Sources* **2018,** 396, 207-212.